water

MDPI

Article

SPH Modelling of Hydraulic Jump Oscillations at an Abrupt Drop

Diana De Padova [1,*], Michele Mossa [1] and Stefano Sibilla [2]

[1] Department of Civil, Environmental, Land, Building Engineering and Chemistry (DICATECh), Polytechnic University of Bari, Via E. Orabona 4, 70125 Bari, Italy; michele.mossa@poliba.it

[2] Department of Civil Engineering and Architecture, University of Pavia, via Ferrata 3, 27100 Pavia, Italy; stefano.sibilla@unipv.it

* Correspondence: diana.depadova@poliba.it

Received: 8 September 2017; Accepted: 11 October 2017; Published: 14 October 2017

Abstract: This paper shows the results of the numerical modelling of the transition from supercritical to subcritical flow at an abrupt drop, which can be characterised by the occurrence of oscillatory flow conditions between two different jump types. Weakly-Compressible Smoothed Particle (WCSPH) model was employed and both an algebraic mixing-length model and a two-equation model were used to represent turbulent stresses. The purpose of this paper is to obtain through the SPH model a deeper understanding of the physical features of a flow, which is, in general, difficult to be reproduced numerically, owing to its unstable character. In particular, the experience already gained in SPH simulations of vorticity-dominated flows allows one to assess the fluctuations of hydrodynamic characteristics of the flow field, (e.g., free surface profile downstream of the jump, velocity, pressure and vorticity). Numerical results showed satisfactory agreement with measurements and most of the peculiar features of the flow were qualitatively and quantitatively reproduced.

Keywords: hydraulic jumps; smoothed particle hydrodynamics models; oscillating characteristics

1. Introduction

A hydraulic jump occurs whenever an upstream supercritical flow is forced to become subcritical. This transition involves a strong energy dissipation, which derives from the increase in turbulence intensity due to the sudden flow deceleration, often resulting in an intense turbulent roller ([1,2]).

A stilling basin is often designed to dissipate the kinetic energy of the flow in a hydraulic jump. Sometimes an abrupt drop is introduced to prevent tailwater effects and to stabilise the jump location. The transition from supercritical to subcritical flow at an abrupt drop affects the design and construction of the stilling basins (e.g., [3–6]).

At an abrupt drop, the transition from supercritical to subcritical flow is characterised by several flow patterns depending upon the inflow and tailwater flow conditions. Figure 1 summarises well acknowledged flow patterns: (1) the A-jump; (2) the wave jump or W-jump; (3) the wave train; (4) the B-jump (or maximum plunging condition) characterised by a plunging jet mechanisms; and (5) the minimum B-jump (or limited jump) with a limited hydraulic jump (e.g., [5]).

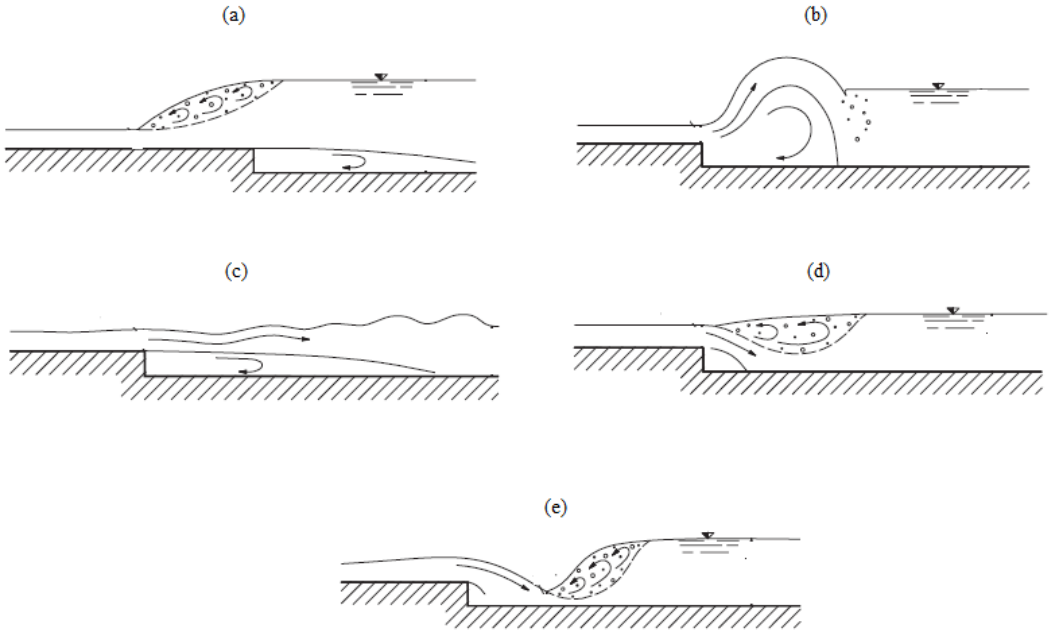

Figure 1. Flow conditions (from Ohtsu and Yasuda, 1991): (**a**) A-jump; (**b**) wave jump; (**c**) wave train; (**d**) B-jump (maximum plunging condition); and (**e**) minimum B-jump (limited jump).

Some researchers pointed out the existence of oscillating phenomena, and particularly of a cyclic variation of jump types over long-lasting experiments, under specific flow conditions (e.g., [5,7–14]).

The oscillating characteristics are usually referred to as a macroscopically visible feature of a hydraulic jump ([12]). These oscillating characteristics can be: (i) change from one type of hydraulic jump to another; (ii) horizontal movement of the jump toe ([15]); (iii) cyclic variation of velocity components and pressure in the region close to the jump roller; and (iv) formation, development and coalescence of the large-scale flow structures. The literature is unclear on the conditions leading to oscillating jumps and cyclic behaviours. Experiments by [3] presented diagrams on the flow patterns as a function of Froude number and dimensionless downstream depth, highlighting some doubts about the existence of the wave- and B-jumps, and these graphs did not mention oscillating characteristics.

The experiments by [16] took into account the previous studies to assess critically the basic flow patterns for the transition from super- to subcritical flows at an abrupt drop and to propose new compelling conclusions regarding the changes of the different types of hydraulic jumps and the variation from one type to another: in particular, it was noted that specific flow conditions can lead to cyclic oscillations between jump types, resulting in the cyclic formation and evolution of jump vortices.

Numerical modelling of a hydraulic jump can be challenging for purely Eulerian or mixed Eulerian–Lagrangian techniques (see, for instance: [17–22]), because of the onset of oscillations, leading to the propagation of short breaking waves which can reduce the accuracy of free-surface capturing schemes [12]. On the other hand, meshless Lagrangian techniques appear in general to be more suitable to capture the complex and highly-unsteady free-surface patterns which characterize a hydraulic jump.

Smoothed Particle Hydrodynamics (SPH) is actually effective in solving fluid-dynamic problems with highly non-linear deformation such as wave breaking and impact ([23–28]); multi-phase flows for coastal and other hydraulic applications with air-water mixtures and sediment scouring ([29–35]); long waves, e.g., floods, tsunamis and landslide submersions ([36,37]); flow around ships and ditching ([38–40]); and oscillating jets inducing breaking waves [41].

In other papers, Smoothed Particle Hydrodynamics (SPH) method has been utilized for modelling of hydraulic jumps with good results. López et al., [42], investigated the capability of the SPH method to reproduce mobile hydraulic jumps with different inflow Fr. Jonsson et al. [43] investigated the

effects of the spatial resolution of the SPH particles and its impact on hydraulic jump behaviour and the conjugate depth. Federico et al. [44] developed a 2D SPH model to enforce inlet and outlet boundary conditions and demonstrated the ability of the SPH method to simulate a hydraulic jump. Chern and Syamsuri [45] displayed the possibility to investigate the effects of a corrugated bed on the hydraulic jump characteristics using SPH. De Padova et al. [46] demonstrated the applicability of the SPH technique to the analysis of three-dimensional (3D) hydraulic jumps in a very large channel, where more complex flow patterns appear. Numerical results showed satisfactory agreement with the laboratory experiments by ([47–49]).

The purpose of this paper is to use a Weakly-Compressible SPH (WCSPH) scheme, together with a suitable turbulence model, to study the oscillating characteristics and cyclic mechanisms in different hydraulic jump types, comparing the results with the laboratory experiments by [16] in order to obtain a deeper understanding of the physical features of the flow.

2. Experimental Set Up

Experimental investigations were carried out in the laboratory of the Department of Civil, Environmental, Land, Building Engineering and Chemistry (hereafter referred to as SIA) of Bari Polytechnic University in a 0.40 m wide, 24.4 m long channel (with sidewalls 0.5 m tall). The walls and bottoms of both channels were made of Plexiglas (Figure 2). The channel hosted in recent years widespread experimental activity on hydraulic jump characterization (see, for instance, [11,12,16,50–52]).

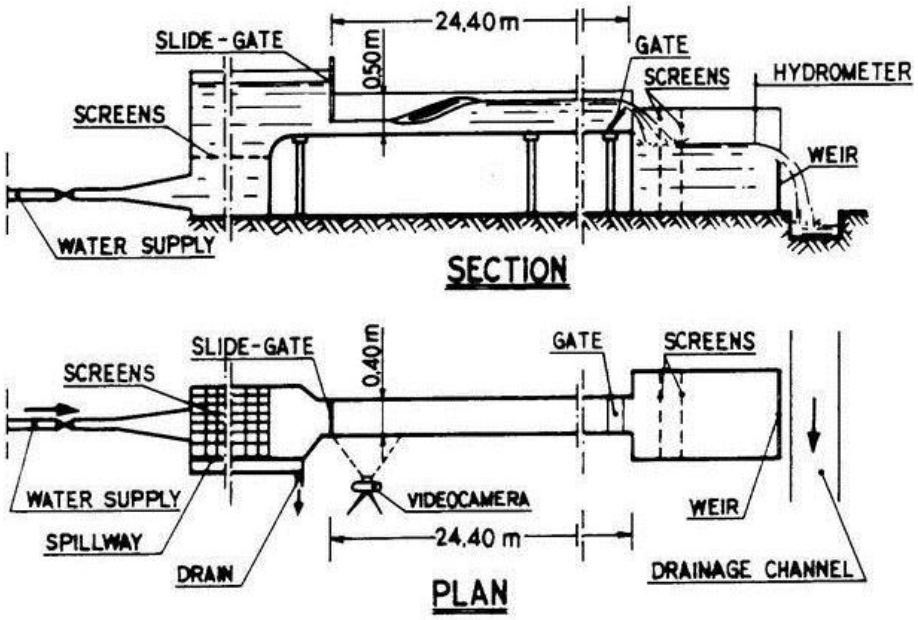

(**a**)

Figure 2. *Cont.*

(**b**)

Figure 2. Channel at the Hydraulics laboratory of the Department of Civil, Environmental, Land, Building Engineering and Chemistry of the Polytechnic University of Bari: (**a**) sketch; and (**b**) picture of the channel.

In the SIA channel, the abrupt drop was made of Plexiglas and located 0.8 m downstream of the gate. The tested elevation drop s was equal to 3.20 or 6.52 cm.

Discharges were measured by a triangular sharp-crested weir. Measurements of upstream and downstream water depths were carried out with electric hydrometers type point gauge supplied with electronic integrators which yielded directly the estimate of the time-averaged flow depth. The hydrometers, supplied with verniers, had a measurement accuracy of $\pm$0.1 mm. Water discharge and tailwater depth were regulated by two gates placed at the upstream and downstream ends of the channel, respectively. For some runs, pressure measurements under the jumps were obtained using a pressure transducer TransInstruments Ltd. type 4310 with a relative pressure difference range equal to 0$\div$7500 Pa. The pressure tap was connected to the transducer using a rigid tube with 2 mm diameter and 0.4 m of length. An amplifier and a conditioner were used to adjust the signal output of the transducer for resolution and acceptable range of the A/D board. In addition, a video camera was used to film the jump for some runs.

Table 1 lists the main experimental parameters of the investigated hydraulic jumps: y_1 is the inflow water depth; y_t is the water depth downstream of the jump; $F_1 = V_1/(gy_1)^{0.5}$ is the inflow Froude number and Re is the Reynolds number defined as $Re = V_1\ y_1/\nu = V_t\ y_t/\nu$ where V_1 and V_t are the flow velocities at water depths y_1 and y_t, respectively, and ν the kinematic water viscosity at the run temperature. Figure 3 shows the locations where y_1 and y_t were measured for each flow pattern i.e., the A-jump and B-jump.

Table 1. Experimental parameters of the analysed hydraulic jumps.

TEST	Run no. (Mossa 2002)	y_1 (cm)	y_t (cm)	V_1 (m/s)	V_t (m/s)	F_1	y_1/y_t	Re	s (cm)	s/y_1	Jump Type
T1	B32	3.5	16.63	1.93	0.41	3.3	4.75	6.10×10^4	3.2	0.9	B-wave
T2	B37	3.7	17.65	1.81	0.38	3	4.76	5.80×10^4	3.2	0.9	A-wave
T3	B38	3.48	1818	1.87	0.36	3.2	5.22	5.90×10^4	3.2	0.9	A-wave
T4	B39	3.14	17.97	2.09	0.36	3.8	5.72	5.70×10^4	3.2	0.9	A-jump
T5	B30	3.19	18.2	2.04	0.36	3.6	5.71	5.90×10^4	3.2	0.9	A-jump
T6	B28	3.78	16.1	1.79	0.42	2.8	4.26	6.10×10^4	3.2	0.9	B-jump (Max.plung.condit.)
T7	B30	3.39	16.78	2.02	0.41	3.5	4.95	6.00×10^4	3.2	0.9	B-jump (Max.plung.condit.)

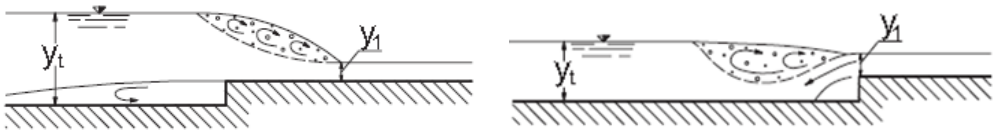

(**a**) (**b**)

Figure 3. Flow conditions: (**a**) A-jump; and (**b**) B-jump (maximum plunging condition).

3. SPH Numerical Method

The SPH meshless, Lagrangian method for the numerical solution of convection–diffusion equations, has been widely applied in the last decades to the simulation of complex, unsteady, free-surface flows.

The reader is referred to textbooks and review articles for a general description of SPH ([53–57]).

The peculiar features of the SPH method used to obtain the present results were described in detail in ([29,46]): simulations are performed through a Weakly Compressible SPH (WCSPH) approach, in which an artificial compressibility is introduced to solve explicitly in time the equations of motion of an incompressible fluid. As suggested by [58], the reduced value of the speed of sound should result in a numerical Mach number everywhere lower than 0.1 in order to bound the error associated with the adoption of a compressible formulation for the incompressible free-surface water flow to 1%: here, the adopted value of 30 ms^{-1} guarantees a numerical Mach number everywhere lower than 0.07.

The Reynolds-averaged Navier–Stokes (RANS) equations in the SPH semi-discrete form become:

$$\begin{cases} \left\langle \frac{D\rho_i}{Dt} \right\rangle = \sum_j m_j (\boldsymbol{v}_i - \boldsymbol{v}_j) \cdot \hat{\nabla} W_{ij} \\ \left\langle \frac{D\boldsymbol{v}_i}{Dt} \right\rangle = -\sum_j m_j \left(\frac{p_i}{\rho_i^2} + \frac{p_j}{\rho_j^2} \right) \nabla W_{ij} + \sum_j m_j (\mathcal{T}_i - \mathcal{T}_j) \cdot \hat{\nabla} W_{ij} + \mathbf{g} \\ p_i - p_0 = c_i^2 (\varrho_i - \rho_0) \\ \mathcal{T}_i = \mu_{T_i} \mathcal{S}_i \end{cases} \quad (1)$$

where the square brackets indicate the SPH approximation for each particle i with mass m_i. The summations are extended to all the particles j at a distance from i smaller than $2h$, i.e., lying within the circle where the adopted C2 Wendland kernel function W_{ij} [59] is defined.

In Eauation (1), $\boldsymbol{v} = (u, v)$ is the velocity vector, p is pressure, ρ is density, $\boldsymbol{g}$ is the gravity acceleration vector, $\mathcal{T}$ is the turbulent shear stress tensor, c is the speed of sound in the weakly compressible fluid, μ_T is the dynamic eddy viscosity, $\mathcal{S}$ is rate-of-strain tensor and the subscript 0 denotes a reference state for pressure computation. All the variables are assumed to be Reynolds-averaged.

The notation $\hat{\nabla} W_{ij}$ in Equation (1) indicates the gradient of W_{ij}, renormalized through a procedure which enforces consistency on the first derivatives to the 1st order [60], leading to a 2nd order accurate discretization scheme in space. The kernel renormalization is applied everywhere, apart from the pressure gradient term, where the form originally proposed by [58] is retained to guarantee momentum conservation.

The semi-discretized system (Equation (1)) is integrated in time by a 2nd order two-stage XSPH explicit algorithm [58], where each particle is moved according to a velocity

$$\boldsymbol{v}_i^X = \varphi_v \sum_j \frac{m_j}{\rho_j} \boldsymbol{v}_j \hat{W}_{ij} + (1 - \varphi_v) \boldsymbol{v}_i^{n+1} \quad (2)$$

where ϕ_v is a velocity smoothing coefficient and $\boldsymbol{v}_i^{n+1}$ is the value obtained by solution of the second equation in Equation (1). The use of XSPH leads to a satisfactory regularization of particle distribution within the computational domain: this regular particle pattern, together with the kernel renormalization procedure described above, leads to computed pressure fields whose energy content at the higher frequencies (i.e., the frequencies mostly connected with numerical noise) is sufficiently

low, as shown in the following Section 4 (see, for instance, Figure 17). The alternative of making use of particle-shifting algorithms, such as those developed for Incompressible SPH ([61] and [62]) and recently extended to WCSPH ([63,64]) was therefore not followed, also considering the problems which might arise at the jump toe, where physical voids arising from wave breaking and air entrainment may be obliterated by an unsuitable particle shifting.

A pressure smoothing procedure is also applied to the difference between the local and the hydrostatic pressure values [46] and contributes to reduce the numerical noise which affects WCSPH owing to high frequency acoustic signals [65]. This approach proved to be effective in SPH analyses of different free-surface flows [29] and constitutes a valid alternative to other methods, such as δ-SPH [66], where a numerical diffusive term for density is added to the continuity equation, or filtering of the high-frequency pressure oscillations ([67,68]).

Two alternative models were tested to estimate the eddy viscosity μ_T:

(1) A mixing-length model ([29,46]), in which $\mu_T = c_\mu \rho l^2 \|\mathcal{S}\|$, where $c_\mu = 0.09$, the mixing-length for each particle is evaluated as:

$$l_i = \min\left[1, \left|\sum_j \frac{m_j}{\rho_j}\nabla W_{ij}\right|^{-3}\right]\min(\kappa y, l_{max}) \tag{3}$$

$\kappa = 0.41$ is the Von Kármán constant, y is the distance from the wall, l_{max} is a cutoff maximum value and the damping function in the first factor of the RHS avoids a non-physical growth of l near the free-surface when the particle distribution is irregular and the SPH evaluation of the gradient of a constant function departs sharply from zero: this function plays therefore a different role than the one of a wake function, such as the one included in the mixing-length model by [69] to simulate turbulent, open-channel uniform flows; the use of a wake function was not considered here because relevant turbulence effects occur mostly close to the hydraulic jump, where the flow conditions are in any case far from uniform;

(2) A SPH version of the standard k-ε turbulence model by [70], in which $\mu_T = c_\mu \frac{k^2}{\varepsilon}$ and the two equations for the turbulent kinetic energy k and for the turbulent dissipation rate ε are:

$$\begin{aligned}\frac{Dk_i}{Dt} &= P_{k_i} + \frac{1}{\sigma_k}\sum_j m_j \frac{\nu_{T_i}+\nu_{T_j}}{\rho_i+\rho_j}\frac{k_i+k_j}{r_{ij}^2+0.01h^2}\boldsymbol{r}_{ij}\cdot\nabla\hat{W}_{ij} - \varepsilon_i \\ \frac{D\varepsilon_i}{Dt} &= C_{\varepsilon_1}\frac{\varepsilon_i}{k_i}P_{k_i} + \frac{1}{\sigma_\varepsilon}\sum_j m_j \frac{\nu_{T_i}+\nu_{T_j}}{\rho_i+\rho_j}\frac{\varepsilon_i+\varepsilon_j}{r_{ij}^2+0.01h^2}\boldsymbol{r}_{ij}\cdot\nabla\hat{W}_{ij} + C_{\varepsilon_2}\frac{\varepsilon_i}{k_i}\sum_j \frac{m_j}{\rho_j}\varepsilon_j\hat{W}_{ij}\end{aligned} \tag{4}$$

where Pk is the production of turbulent kinetic energy depending on the local rate of deformation and ν_T is the eddy viscosity. As in [71], the values originally proposed by [70] for the model constants ($\sigma_k = 1$, $\sigma_\varepsilon = 1.3$, $C_{\varepsilon 1} = 1.44$, $C_{e2} = 1.92$) were maintained here.

Wall boundary conditions are imposed by the *ghost particle* method [72], while supercritical inflow conditions are obtained by introducing a $2h$-wide layer of fluid particles with constant velocity and head along the water depth.

The inflow condition is enforced through the introduction of a $2h$-wide layer of fluid particles, arranged on a regular grid and moving with constant velocity V_1 and head y_1: a new row of particles is created upstream of the layer at each Σ/V_1 time interval, Σ being the initial particle spacing. The k and ε values at the inflow are computed by assuming a constant 10% turbulence intensity and a mixing length equal to $0.5\, y_1$.

An outflow velocity V_t and head y_t are imposed to each particle crossing the outflow boundary, and these values are kept frozen in the $2h$-wide outflow buffer layer, so that their motion is maintained

at constant speed: when the particles exit the buffer layer, they are removed from the computation; k and ε values are also frozen in the buffer layer.

For velocity and head, these inflow/outflow conditions are basically analogous to the ones described by [44].

4. Numerical Tests and Results

Seven hydraulic jumps with Froude number ranging 2.8–3.9 were investigated in a rectangular channel. The geometrical setup was based on the experimental study by [16], who focused on the oscillating changes of the different types of hydraulic jumps (variation from one type to another). See Table 1 for experimental data.

For all seven tests, the numerical domain was 2 m long and 0.4 m high, shorter than the real channel in the test facility. The shorter domain was chosen to reduce the computational cost without influencing the quality of the numerical solution, as shown by [46] in the case of 2D undular jump simulations. A schematic figure of the problem setup can be seen in Figure 4.

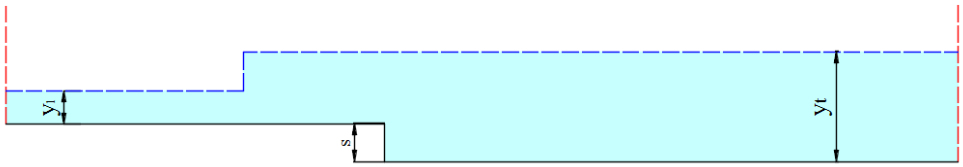

Figure 4. Schematic figure of the geometrical setup. Solid black lines indicates solid walls, dashed blue lines the initial free surface and dashed red lines show the position of the periodic open boundaries.

A thorough sensitivity analysis was already performed by the authors in the application of the same SPH numerical method to hydraulic jumps and breaking wave flows ([29,46]): according to this analysis, the SPH simulations of the cases here studied were performed by adopting a velocity smoothing coefficient in the XSPH scheme $\phi_v = 0.01$. The ratio of the smoothing length to the initial particle spacing Σ was maintained to a constant value of $\eta/\Sigma = 1.5$ [73] for all the simulations. A convergence analysis was carried out by choosing different initial particle spacing Σ ranging from 0.015 to 0.005 m. The related number of SPH particles N_P in the computational domain ranged from about 1000 to 9000, respectively. It can be seen that the simulation at the lowest resolution is not able to predict the oscillating characteristics and cyclic mechanisms in hydraulic jumps (Figure 5).

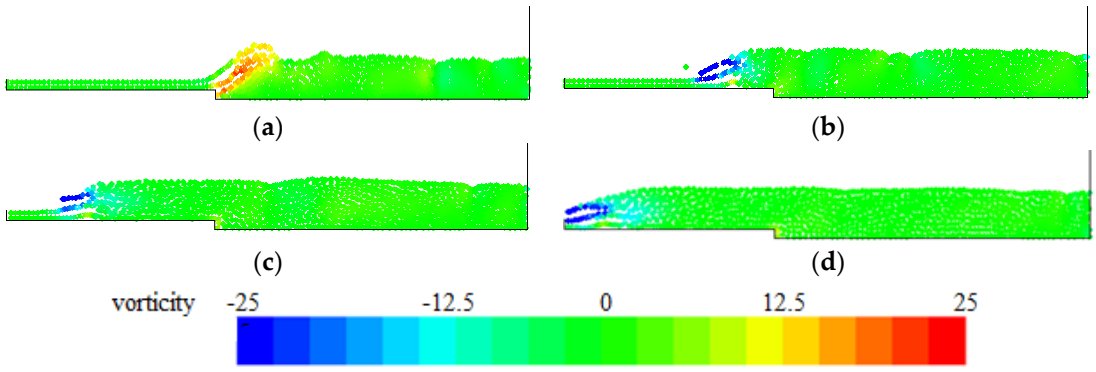

Figure 5. Instantaneous SPH vorticity field in the SPH simulation of Test T1a with an initial particle spacing equal to 0.015: (**a**) t = 6 s; (**b**) t = 9 s; (**c**) t = 12 s; and (**d**) t = 15 s. Vorticity values in the colour scale are expressed in s^{-1}.

Figure 6 shows that an initial particle spacing $\Sigma \leq 0.010$ m guarantees the independence of the SPH result from the resolution and yield a result in accordance with the experiments.

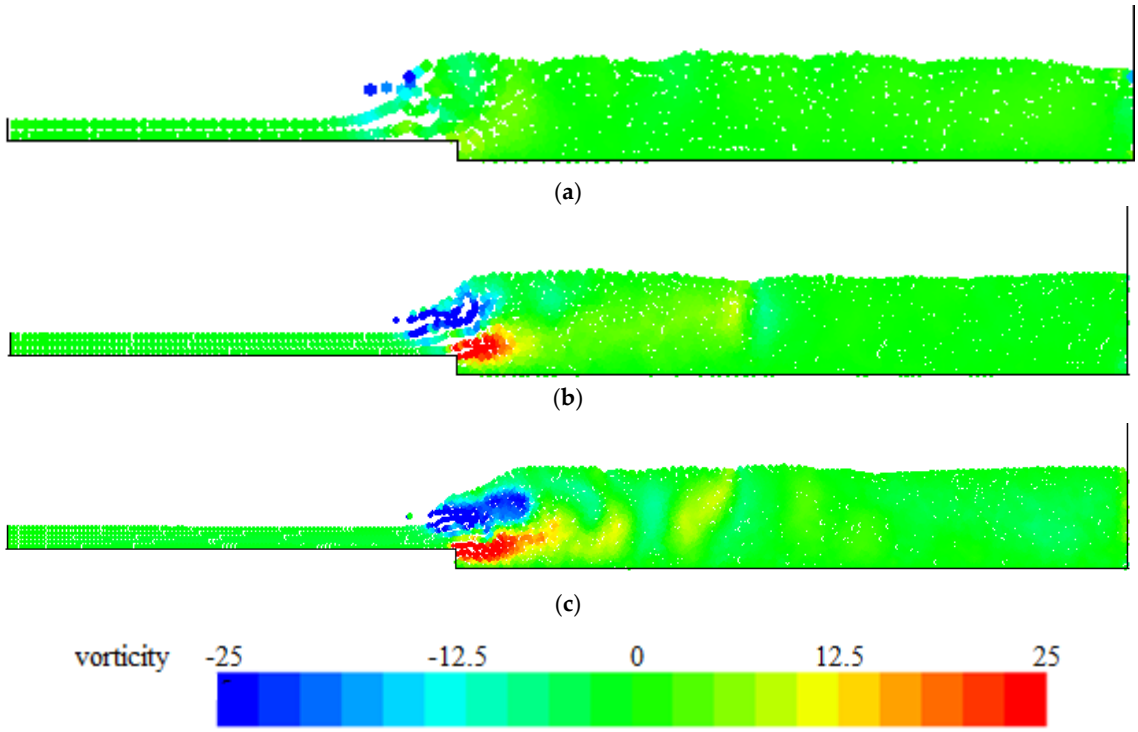

Figure 6. Instantaneous SPH vorticity field (t = 8 s) in the SPH simulation of Test T1 with different particle resolutions: (**a**) Σ = 0.015 m; (**b**) Σ = 0.010 m; and (**c**) Σ = 0.005 m. Vorticity values in the colour scale are expressed in s^{-1}.

The sensitivity analysis highlights that, with a value of an initial particle spacing $\Sigma \leq 0.010$ m, SPH simulations show results in accordance with the experiments. Therefore, all the SPH simulations have been then performed with an initial particle spacing Σ = 0.010 m and η/Σ = 1.5.

Sensitivity to the turbulence model was also investigated and, similarly to the analysis shown by De Padova et al. (2013), test T1 was repeated by adopting both a mixing length turbulence model with $l_{max} = 0.5\, h_2$ and the two-equation model (10). Table 2 summarizes the principal characteristics of the simulations in the sensitivity analysis.

Table 2. Numerical parameters of the SPH simulations in the sensitivity analysis.

TEST	Turbulence Model	η/Σ	N_P
T1a	mixing-length model	1.5	3000
T1b	k-ε turbulence model	1.5	3000

Both the mixing length model and the k-ε model yield similar results and are able to predict the oscillating characteristics and cyclic mechanisms in hydraulic jumps.

The instantaneous vorticity fields (Figures 7 and 8) of the configuration with oscillations between the B and wave jump clearly indicate that the transition phase between the two jump types is well reproduced by both turbulence models (T1a and T1b). Vortices are characterized by a clockwise or anti-clockwise rotation, depending on which type of jump is present. In particular, vortices are characterized by a clockwise rotation when the wave jump occurs (Figures 7a–c and 8a–c) and by an anti-clockwise one for the B jump (Figures 7b–d and 8b–d), respectively.

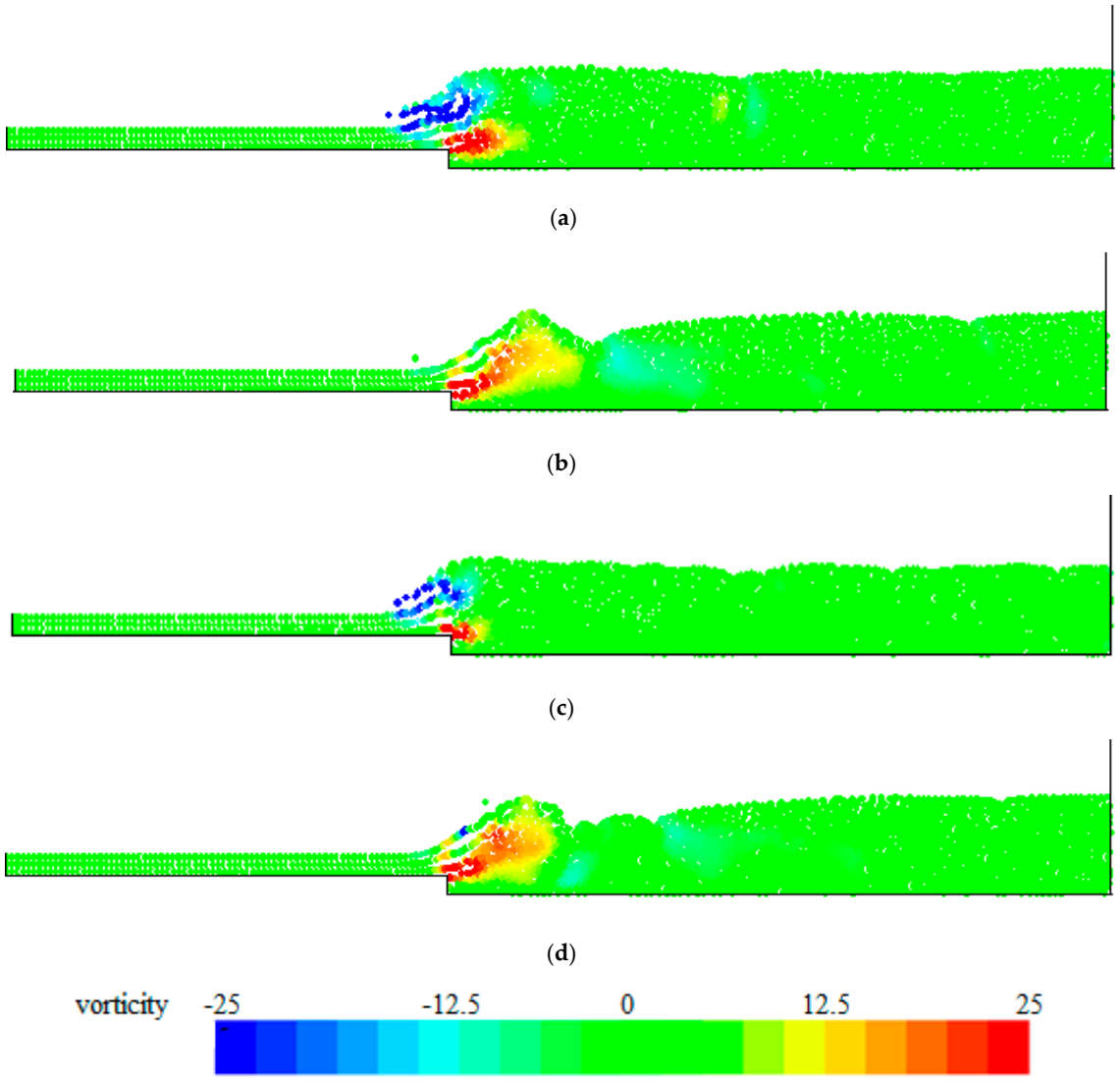

Figure 7. Instantaneous SPH vorticity field in the SPH simulation of Test T1a: (**a**) t = 8 s; (**b**) t = 17 s; (**c**) t = 22 s; and (**d**) t = 27 s. Vorticity values in the colour scale are expressed in s^{-1}.

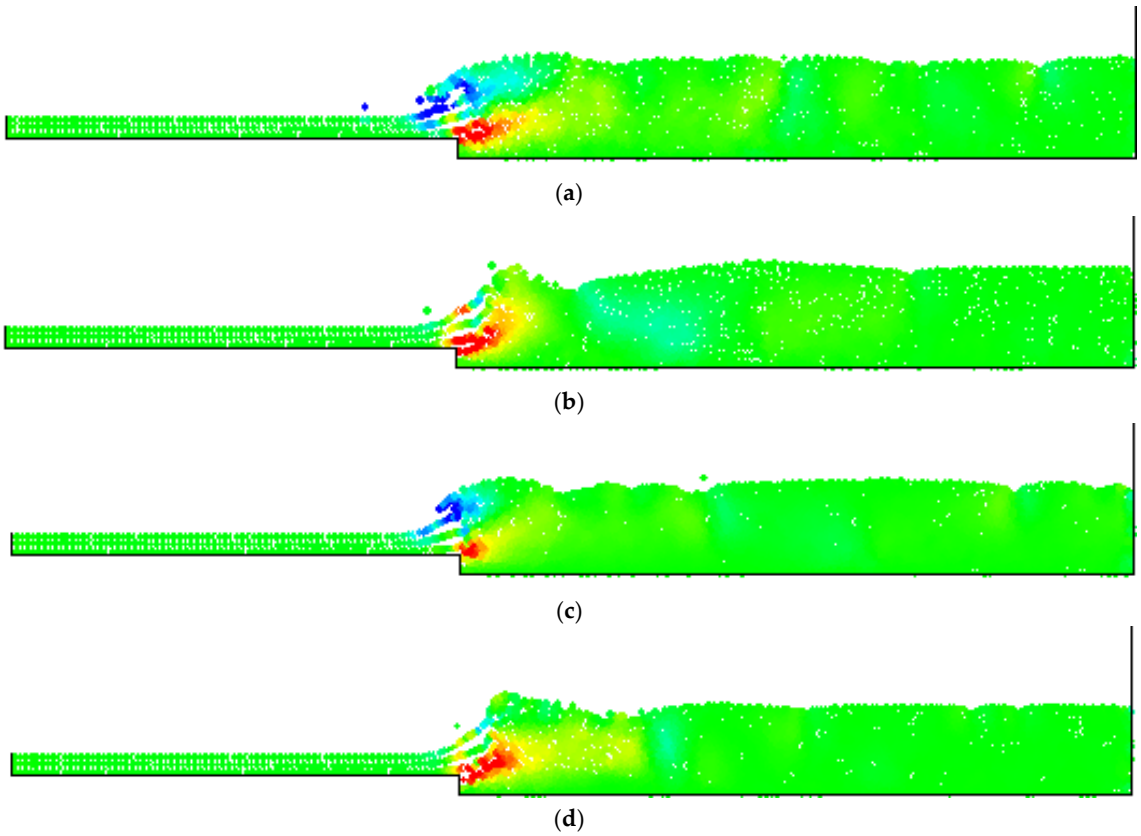

Figure 8. Instantaneous SPH vorticity field in the SPH simulation of Test T1b: (**a**) t = 15 s; (**b**) t = 21 s; (**c**) t = 26 s; and (**d**) t = 30 s. Colour scale is the same as in Figure 7.

Figure 9 shows the amplitude spectrum of the pressure fluctuations computed in tests T1a and T1b, compared with the measurements under the hydraulic jump B32 of Table 1, where the pressure tap was located at a distance of 26 cm from the time-averaged position of the jump toe. From the analysis of the spectrum, it is clear that even the pressure fluctuations are quasi-periodic and strongly influenced by the oscillations between the B and wave jump types; furthermore, it is possible to observe the existence of a peak in each spectrum, as was shown in the experiments by [16].

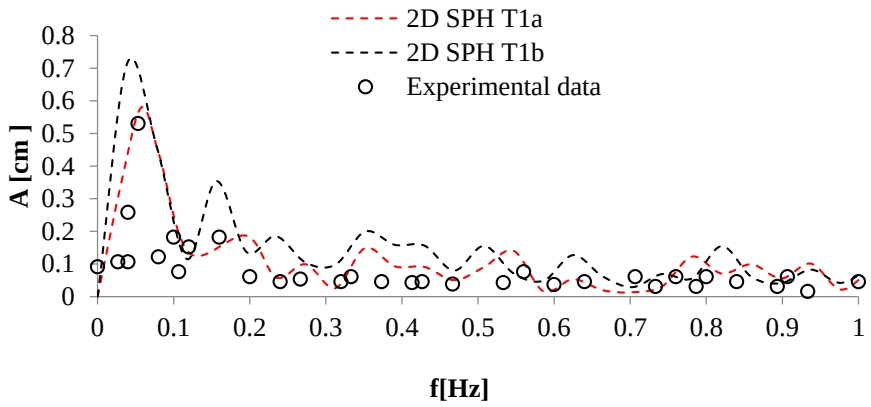

Figure 9. Amplitude spectrum of pressure fluctuations under the hydraulic jump (configuration B32 of Table 1) for the SPH simulations of test T1 and two different turbulence models: mixing-length (T1a) and k-ε (T1b).

Although both turbulence models yield similar results, the detailed comparison of the computed amplitude spectra with the measured ones shows that the results obtained with the mixing-length model are closer to the experimental data than the *k*-ε ones (Figure 9). In particular, the two-equation turbulence model overestimates the peak amplitude of the pressure fluctuations upstream, while predicting a lower main frequency. A possible explanation of this behaviour could reside in an underprediction of turbulent kinetic energy (or in an overprediction of it dissipation rate) by the *k*-ε model, which leads to a slightly lower turbulent diffusion downstream of the jump. A possible solution to these problems could be found in a careful tuning of the model parameters, or in the application of a different two-equation model, such as the RNG k-ε model, which has been successfully applied to the Eulerian numerical simulations of hydraulic jumps [22]. However, the obtained results showed that a good agreement with experiments could be already obtained by applying the simpler, mixing-length turbulence model and, therefore, all the remaining SPH simulations (tests T2 to T7) were performed with it.

Analysis of Stable vs. Oscillating Flow Behaviour

The simulated flow patterns reproduce what was observed during the experiments.

The stable states shown by tests T4 and T6 are confirmed by the numerical results, showing the formation of an A-jump for test T4 (Figure 10) and of a B-jump for test T6 (Figure 11), respectively: although the jump toe exhibits a certain displacement from its average position, the jump pattern is maintained during the whole simulation period.

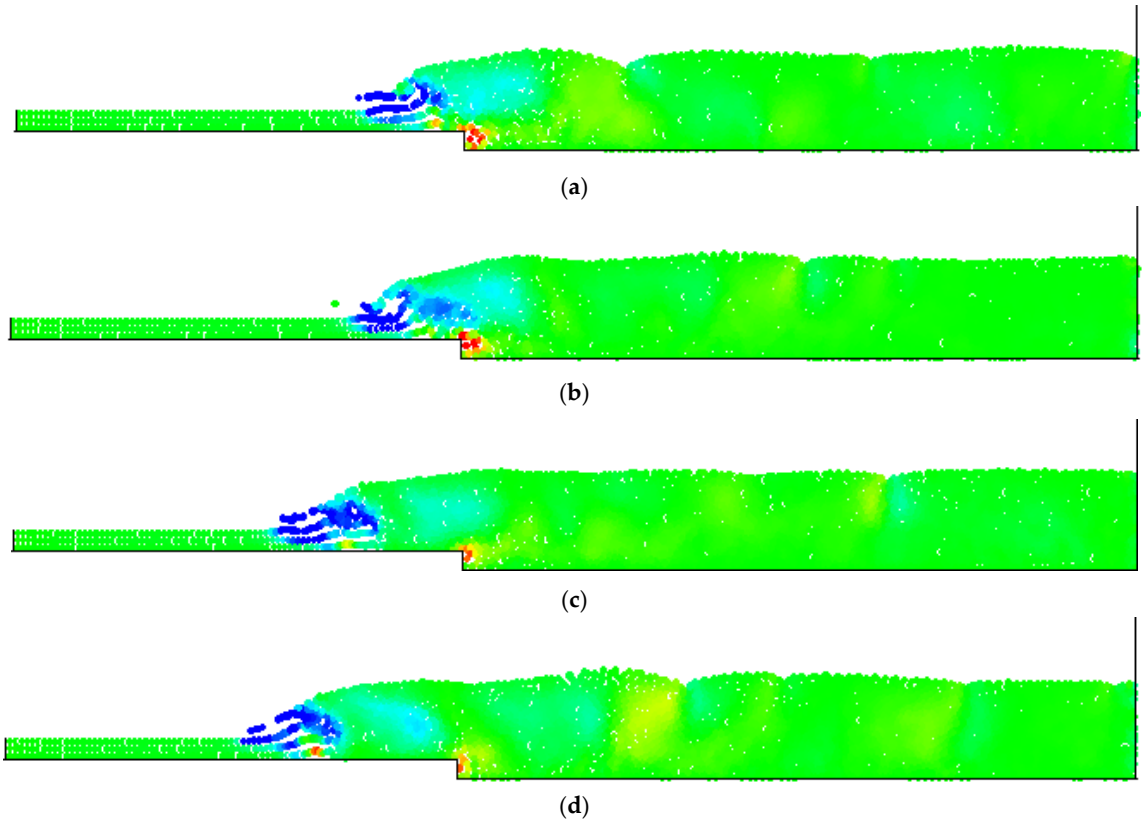

Figure 10. Instantaneous SPH vorticity field in the SPH simulation of Test T4: (**a**) t = 15 s; (**b**) t = 18 s; (**c**) t = 22 s; and (**d**) t = 24 s. Colour scale is the same as in Figure 7.

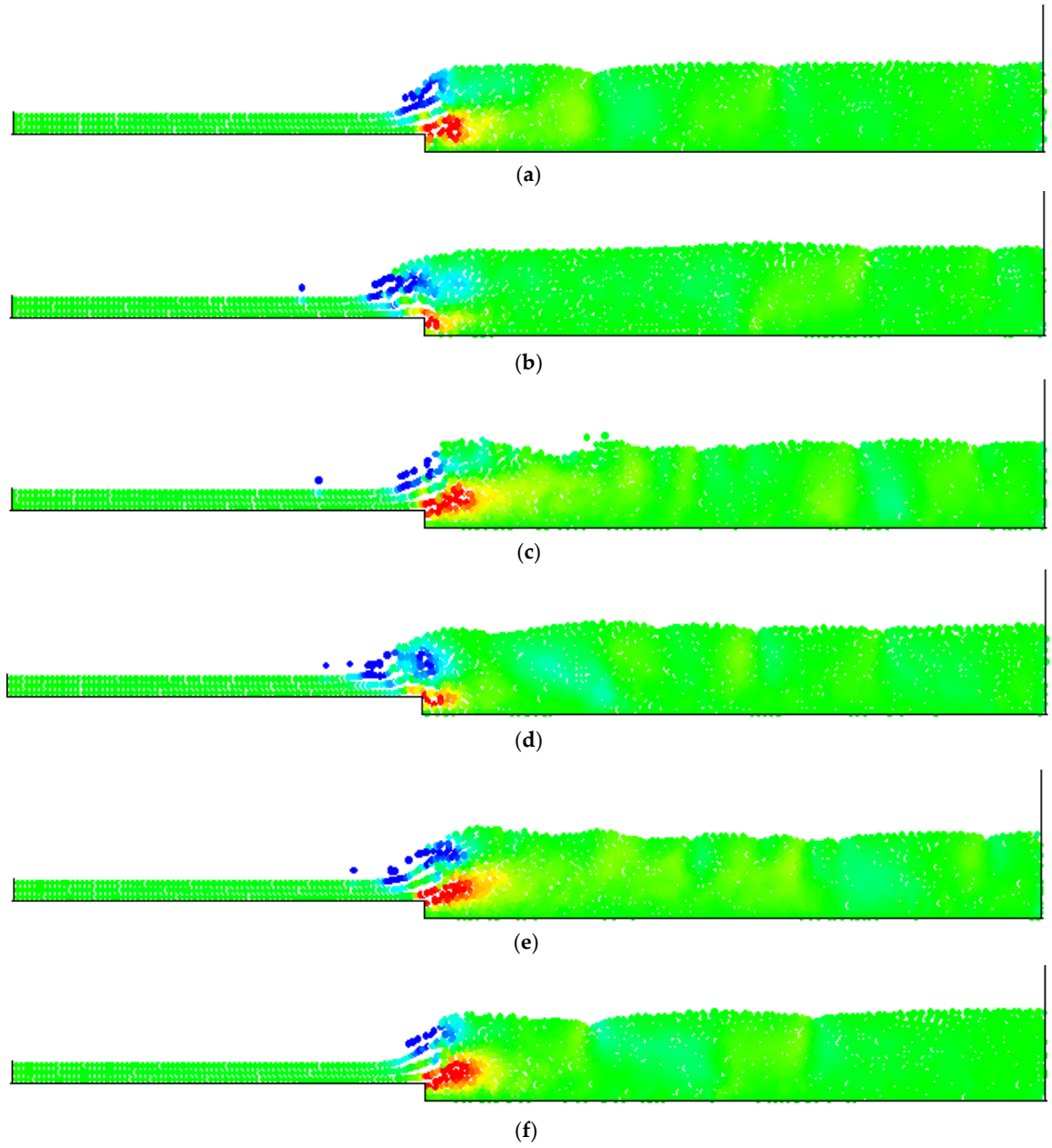

Figure 11. Instantaneous SPH vorticity field in the SPH simulation of Test T6: (**a**) t = 30 s; (**b**) t = 40 s; (**c**) t = 50 s; (**d**) t = 60 s; (**e**) t = 70 s; and (**f**) t = 80 s. Colour scale is the same as in Figure 7.

For the flow conditions that exhibited an oscillatory pattern in the experiments, oscillatory flow patterns were also observed during numerical simulations, such as for test T2, where an A-wave pattern occurs (Figure 12), or for the test T1 previously discussed, which shows a B-wave behaviour (Figure 7).

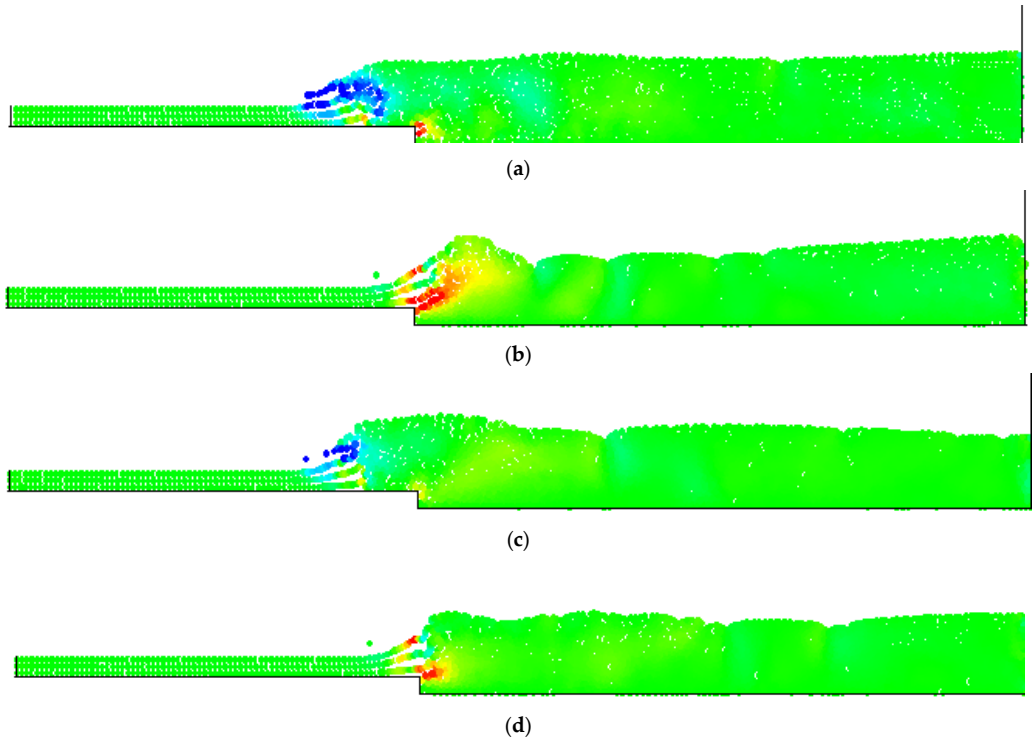

Figure 12. Instantaneous SPH vorticity field in the SPH simulation of Test T2: (**a**) t = 5 s; (**b**) t = 10 s; (**c**) t = 12 s; (**d**) t = 16 s; Colour scale is the same as in Figure 7.

The previous results show that the SPH simulations can correctly reproduce all the main characteristics of this phenomenon, which under specific flow conditions can lead to cyclic oscillations between jump types, resulting in the cyclic formation and evolution of jump vortices. As such, the complete spatial and temporal knowledge of the flow yielded by the SPH simulation can help us to improve the understanding of the phenomena by performing additional analyses of the flow field, without requiring new extensive experimental activity.

Figure 13 shows the amplitude spectra of the time series of the surface elevations, upstream and downstream of the jump for test T1. From the analysis of these spectra it is possible to observe in each of them the existence of a peak at a frequency around 0.1 Hz, which confirms the conclusions drawn by [12], who stated the quasi-periodicity of the oscillating characteristic of wave and B jumps.

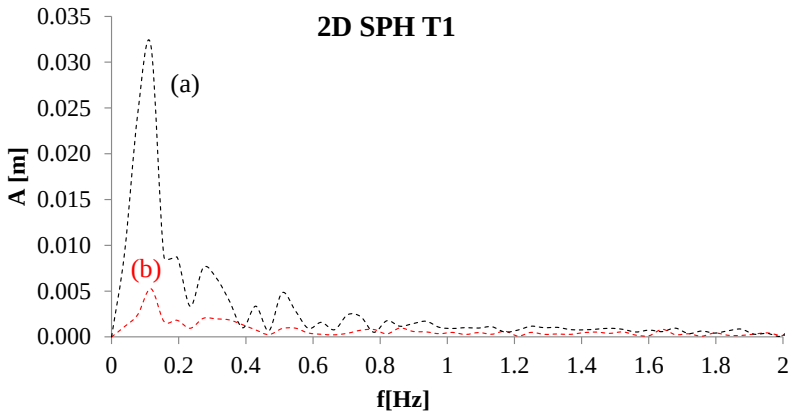

Figure 13. Test T1: Amplitude spectrum of the time series of the surface elevations: (**a**) upstream; and (**b**) downstream of the jump.

Furthermore, as the frequency of the peak in the upstream spectrum is almost equal to the downstream one, it is possible to conclude that fluctuations of the surface profile downstream of the jump also depend essentially on the alternations between B and wave jumps.

Figure 14 shows the amplitude spectrum of the time series of the surface elevations, upstream and downstream of the jump for test T2. From the analysis of the previously mentioned figure it is possible to observe the also in this case the existence of a peak in the spectrum of the time series of the surface elevations upstream of the jump, consistently with the oscillations between A and wave jumps.

However, in this case, no dominant peak frequency was noted, unlike in the T1 case with alternations between B and wave jumps. Consequently, as also suggested by [12], the present numerical results confirm that the surface profile downstream of the roller in this case is not affected strongly by the oscillation between different jump types.

It is possible to evaluate non-linearity through the ratios between the amplitude of the two higher harmonics (A2 and A3) and that of the main component (A1), as proposed by [74,75]. A value of A2/A1 equal to 0.105 and 0.017 is found for surface elevation upstream of the jump in test T1 and test T2, respectively. A value of A3/A1 equal to 0.12 and 0.25 is found for surface elevation upstream of the jump in test T1 and test T2, respectively.

A value of A2/A1 equal to 0.18 and 0.35 is found for surface elevation downstream of the jump in test T1 and test T2, respectively. A value of A3/A1 equal to 0.35 and 1.056 is found for surface elevation downstream of the jump in test T1 and test T2, respectively. The tendency of these ratios to increase in the direction of the flow shows that the non-linearity of the surface waves tends to enhance while the waves propagate downstream.

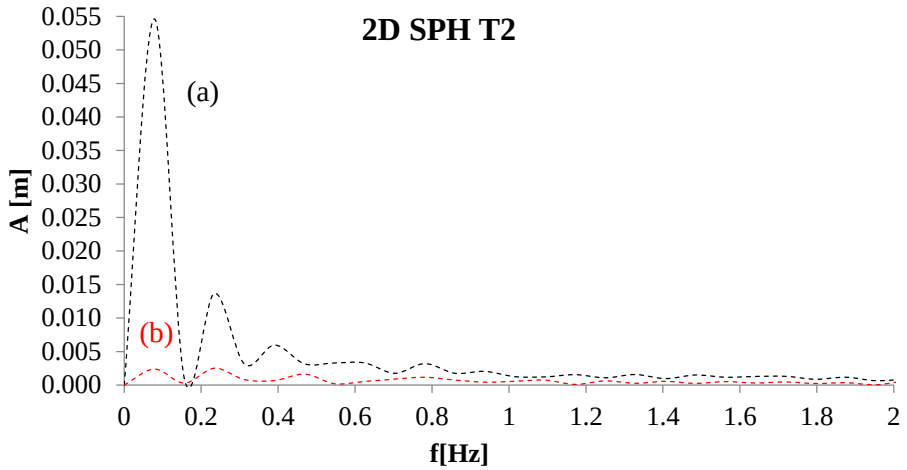

Figure 14. Test T2: Amplitude spectrum of the time series of the surface elevations: (**a**) upstream; and (**b**) downstream of the jump.

The numerical results highlight also the relationship between the tailwater depth ratio y_t/y_1 and the upstream Froude number F_1 as a function of the relative step height s/y_1. The results are presented in the form of diagram (Figure 15) as function of the relative step height s/y_1 equal to 0.06 to 0.1. In the diagram (Figure 15), the basic flow pattern is indicated in the legend (A-jump, B-jump) including the oscillatory flow patterns (B-wave and A-wave).

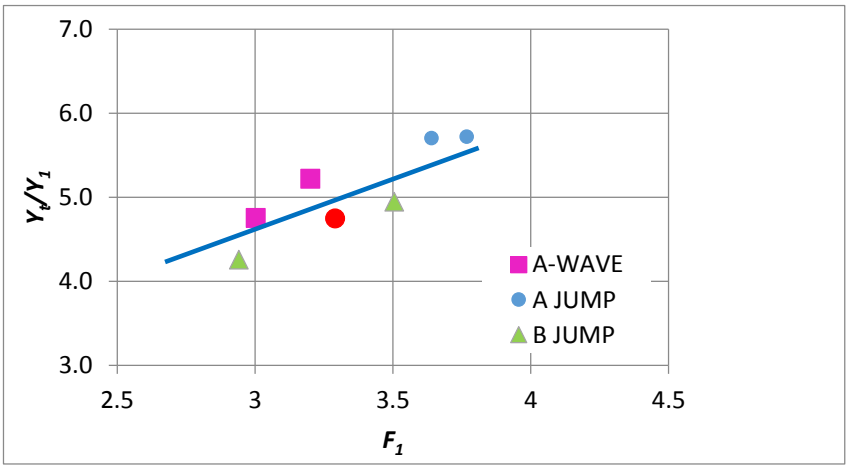

Figure 15. Regime chart for flow configurations with $0.6 < s/y_1 < 1.1$. The dashed line shows the approximate boundaries between A and B jump types.

The results show the different regions of flow conditions and the occurrence of oscillatory flow conditions between two different jump types characterised by quasi-periodic oscillations (Figure 15).

Figures 16–19 show a part of the time series and the amplitude spectra of the pressure evaluated at different locations along the channel the bottom under the hydraulic jumps T1and T2 of Table 1, which represent the two possible oscillating regimes (B-wave and A-wave, respectively). In particular, the pressure was evaluated at a distance of 7, 10, 20 and 100 cm from the time-averaged position of the hydraulic jump toe.

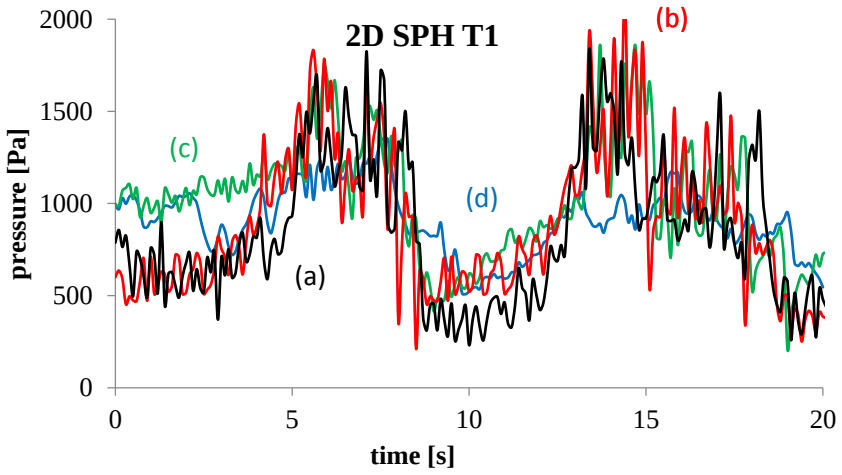

Figure 16. Time series of the pressure under hydraulic jump (configuration: T1) at a distance of: (**a**) 7 cm; (**b**) 10 cm; (**c**) 20 cm; and (**d**) 100 cm, from the time-averaged position of the hydraulic jump toe.

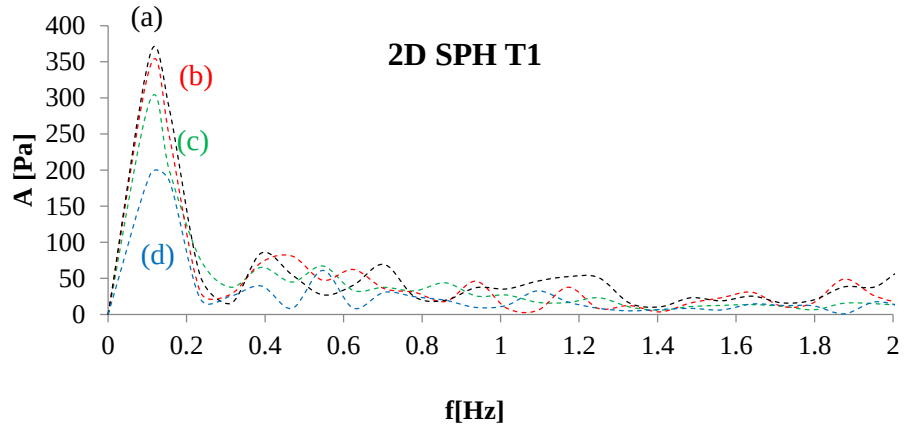

Figure 17. Amplitude spectrum of pressure fluctuations under hydraulic jump (configuration: T1) at a distance of: (**a**) 7 cm; (**b**) 10 cm; (**c**) 20 cm; and (**d**) 100 cm, from the time-averaged position of the hydraulic jump toe.

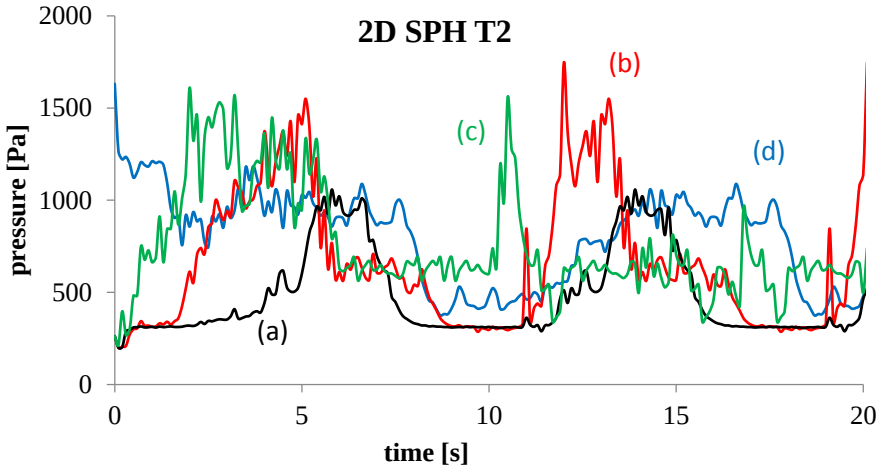

Figure 18. Time series of the pressure under hydraulic jump (configuration: T2) at a distance of: (**a**) 7 cm; (**b**) 10 cm; (**c**) 20 cm; and (**d**) 100 cm, from the time-averaged position of the hydraulic jump toe.

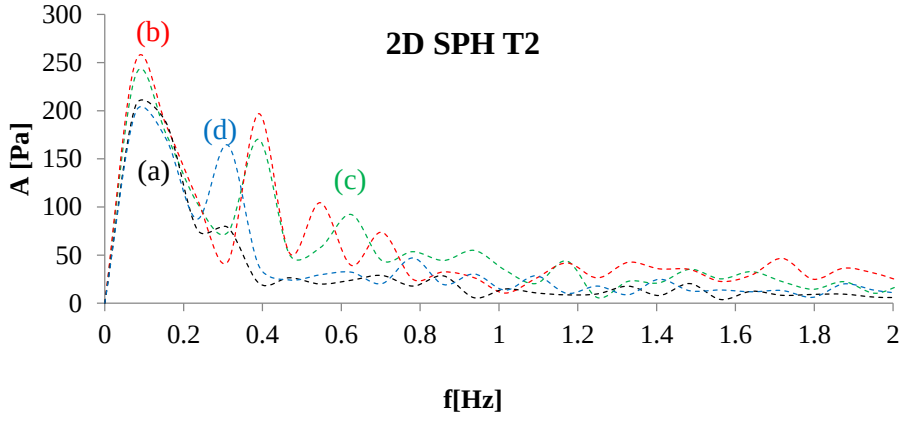

Figure 19. Amplitude spectrum of pressure fluctuations under hydraulic jump (configuration: T2) at a distance of: (**a**) 7 cm; (**b**) 10 cm; (**c**) 20 cm; and (**d**) 100 cm, from the time-averaged position of the hydraulic jump toe.

It can be seen from the pressure time history that, in the point closest to the jump toe, the bottom pressure assumes alternatively low and high pressures which can be mostly related to low and high water levels. Downstream, the cycle between low and high pressures is less regular, possibly because of the simultaneous effect of level fluctuations due to waves and of turbulent pressure fluctuations downstream of the roller. From the analysis of the pressure amplitude spectra for test T1 (Figure 17), it is clear that even the pressure fluctuations are quasi-periodic and strongly influenced by the oscillations between the B and wave types, as they show a peak amplitude at the same frequency of the elevation spectra.

For the test T2 (Figure 19), no dominant peak frequency was noted, unlike in the T1 case with alternations between B and wave jumps.

Figures 20–23 show a part of the time history of the horizontal u and vertical v velocity components computed at a point 0.01 m above the channel bottom under the hydraulic jumps T1 and T2 of Table 1, at a distance of 7, 10, 20 and 100 cm from the time-averaged position of the hydraulic jump toe.

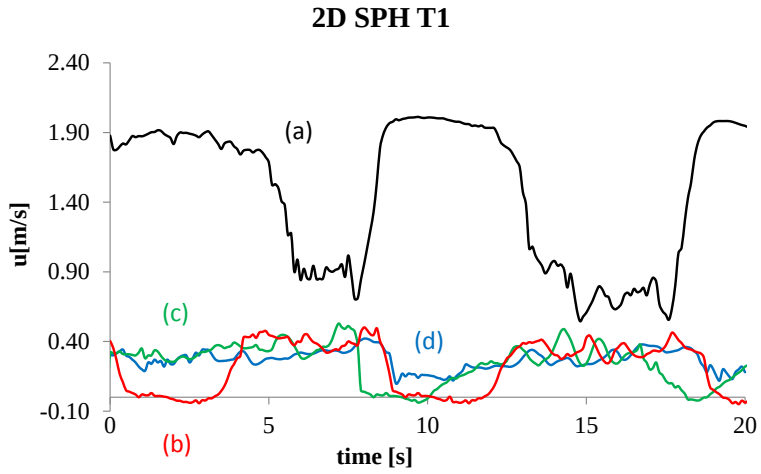

Figure 20. Time series of the horizontal velocity component under hydraulic jump (configuration: T1) measured at a distance of: (**a**) 7 cm; (**b**) 10 cm; (**c**) 20 cm; and (**d**) 100 cm, from the time-averaged position of the hydraulic jump toe.

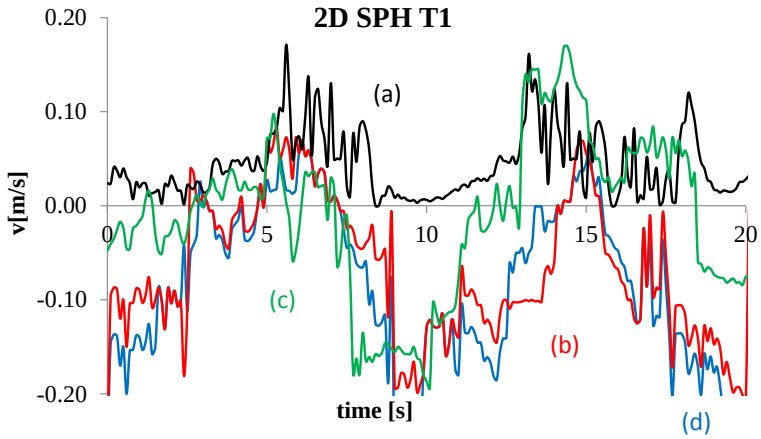

Figure 21. Time series of the vertical velocity component under hydraulic jump (configuration: T1) measured at a distance of: (**a**) 7 cm; (**b**) 10 cm; (**c**) 20 cm; and (**d**) 100 cm, from the time-averaged position of the hydraulic jump toe.

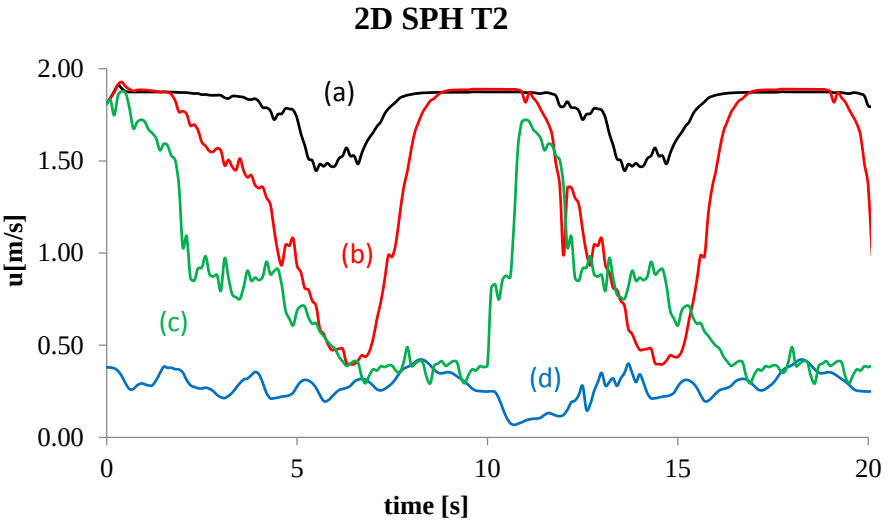

Figure 22. Time series of the horizontal velocity component under hydraulic jump (configuration: T2) measured at a distance of: (**a**) 7 cm; (**b**) 10 cm; (**c**) 20 cm; and (**d**) 100 cm, from the time-averaged position of the hydraulic jump toe.

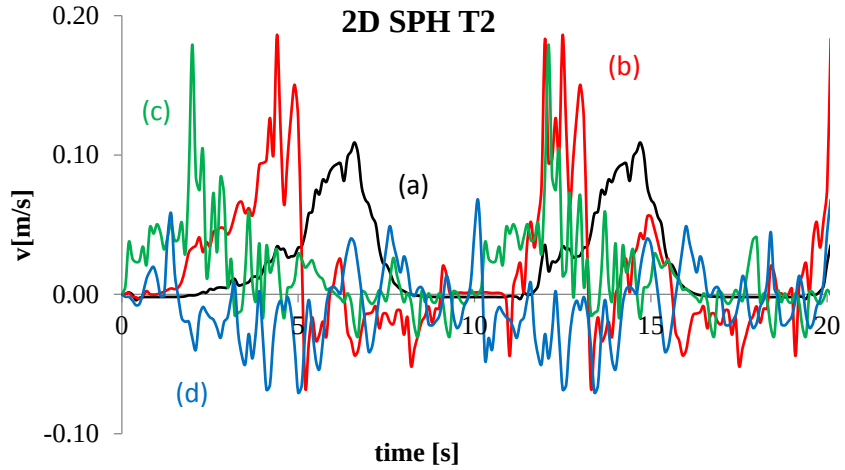

Figure 23. Time series of the vertical velocity component under hydraulic jump (configuration: T2) measured at a distance of: (**a**) 7 cm; (**b**) 10 cm; (**c**) 20 cm; and (**d**) 100 cm, from the time-averaged position of the hydraulic jump toe.

The basic characters of the oscillating flow fields depicted in Figures 5 and 10 can be easily deduced from the velocity time histories.

In the case of test T1, the B-jump phase conserves a non-zero horizontal velocity component throughout the jump, consistent with the presence of the anti-clockwise roller on the surface; on the other hand, the wave-phase exhibits an almost vertical, downward flow at the intermediate locations downstream of the jump, which are a consequence of the strong clockwise roller, as sketched in Figure 1b.

In the case of test T2, the oblique flow induced by the jump roller just downstream of the toe during the A-jump phase (Figure 1a) can be deduced by the reduced values of u and by the positive values of v, while the structure of the wave-jump phase is less defined than in the previous case.

In any case, the analysis of the oscillating phenomena indicates in both oscillating flows a strong correlation among the surface profile elevations, velocity components and pressure fluctuations.

A quantitative evaluation of this correlation can be obtained by computing the correlation coefficient r:

$$r = \frac{\sum_{i=1}^{n} \left[\left(x_{1_i} - \overline{x_1} \right) \left(x_{2_i} - \overline{x_2} \right) \right]}{\sqrt{\sum_{i=1}^{n} \left(x_{1_i} - \overline{x_1} \right)^2 \sum_{i=1}^{n} \left(x_{2_i} - \overline{x_2} \right)^2}} \quad (5)$$

where x_1 and x_2 are the two variables values, and the bar denotes an average of the two variables values.

For test T1, the computed values of r for (p–u), (p–v) and (u–v) pairs of data at a distance of 7 cm from the time-averaged position of the hydraulic jump toe, are equal to −0.72, 0.85 and −0.8, respectively (Figure 24).

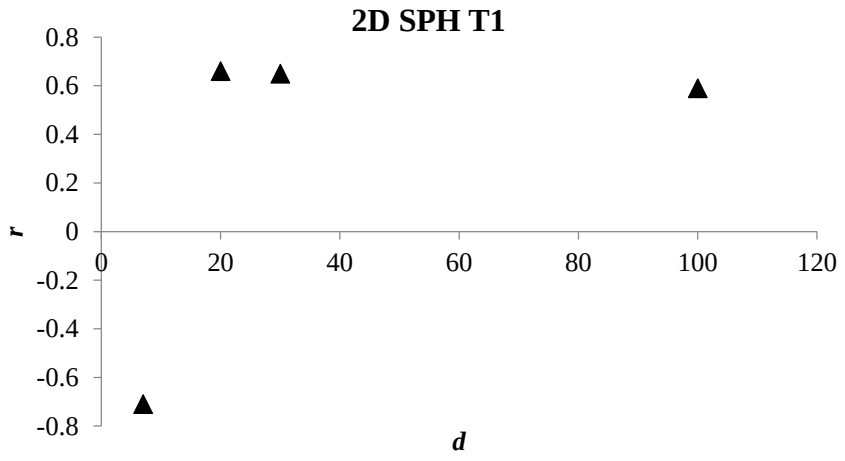

(**a**)

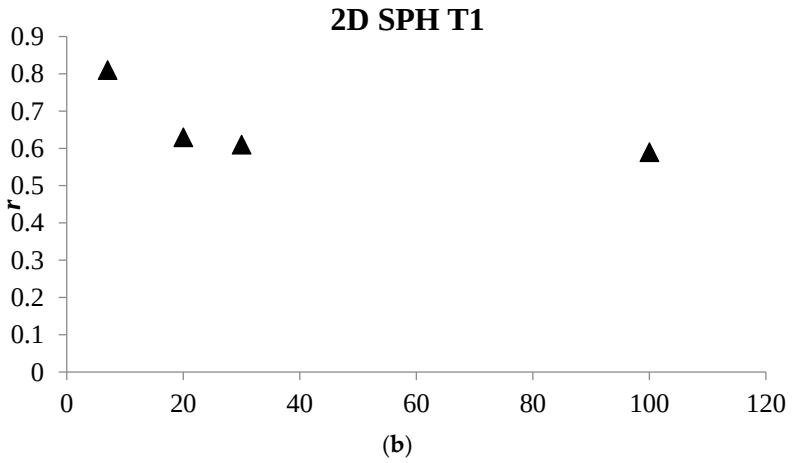

(**b**)

Figure 24. *Cont.*

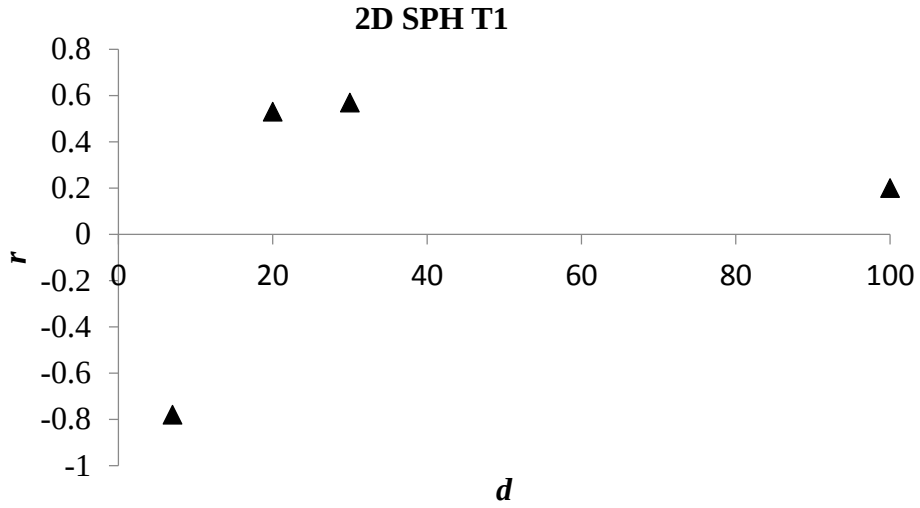

(**c**)

Figure 24. Plot of ***r*** versus ***d*** for: (**a**) (*p*–*u*); (**b**) (*p*–*v*); and (**c**) (*u*–*v*) pairs of data (configuration: T1).

For test T2, the computed values of *r* for (*p*–*u*), (*p*–*v*) and (*u*–*v*) pairs of data at a distance of 7 cm from the time-averaged position of the hydraulic jump toe, are equal to −0.98, 0.97 and −0.96, respectively (Figure 25).

High negative values of the *r* coefficient for (*p*–*u*) indicate that, in general, upstream of the bottom step low levels correspond to horizontal flow (wave-jump conditions) and vice versa. This anti-correlation between pressure (or level) and *u* fluctuations is maintained downstream in the T2 case, while in the T1 case the two quantities are instead weakly correlated.

Farther downstream, the two velocity components and the pressures are substantially uncorrelated in the T2 case, indicating that the characteristic flow pattern of alternate near-wall and subsurface streams does not imply any preferential direction of the vertical motions, while exhibit still a non-zero degree of correlation in the T1 case, indicating that the oscillation between the B-jump and the stronger wave-jump tends to propagate its effects more than the oscillation between wave-jump and A-jump.

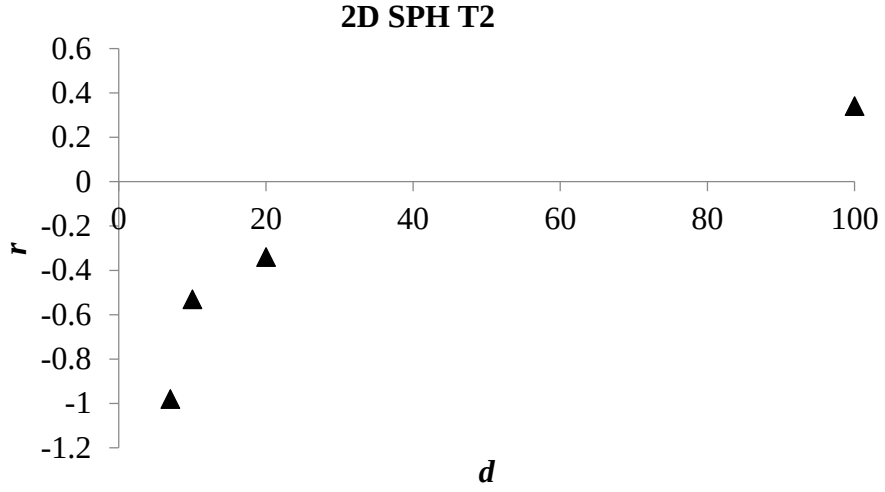

(**a**)

Figure 25. *Cont.*

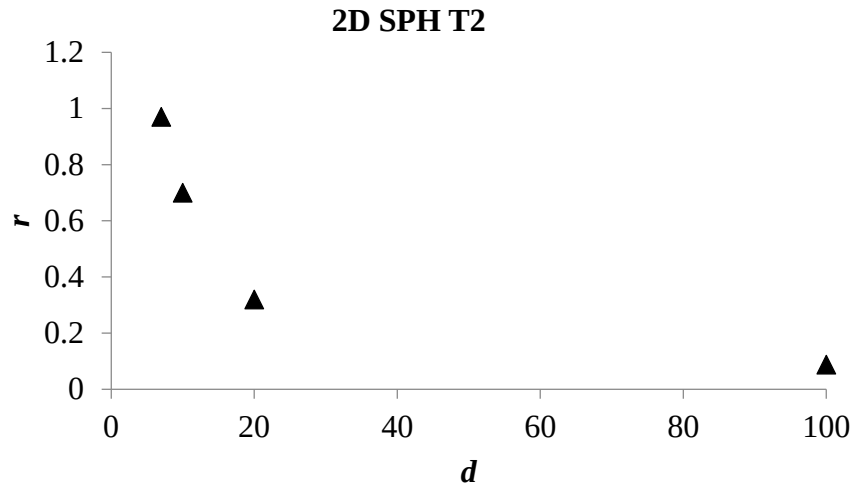

(**b**)

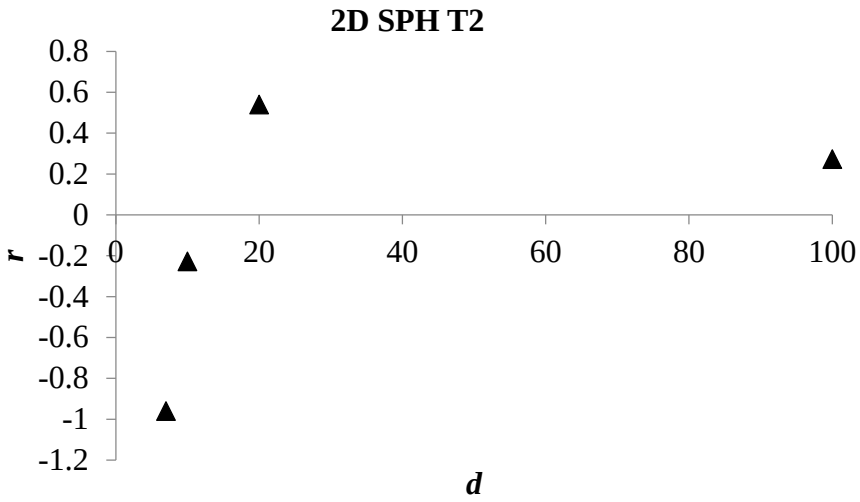

(**c**)

Figure 25. Plot of ***r*** versus ***d*** for: (**a**) (p–u); (**b**) (*p*–*v*); and (**c**) (*u*–*v*) pairs of data (configuration: T2).

5. Conclusions

A Weakly-Compressible SPH (WCSPH) scheme, which includes both an algebraic mixing-length model and a two-equation turbulence model, was applied to the modelling of the transition from supercritical to subcritical flow at an abrupt drop, which can be characterised by several flow patterns depending upon the inflow and tailwater flow conditions.

The numerical results showed a satisfactory agreement with the measurements by [16] and most of the peculiar features of the flow were qualitatively and quantitatively reproduced by the SPH model. It must be highlighted that the analysis of the sensitivity of the present results to the particle resolution showed the limits that allow one to obtain a precise description of the main characteristics of these hydraulic jumps, even if the precise detail of the turbulent flow inside the jump roller is not described. From this viewpoint, a valuable outcome of the present research is the demonstration that the SPH method, being able to represent the onset of the different oscillating regimes, can yield results whose reliability goes beyond the simple validation of a numerical scheme, to a point where the data obtained

by the simulation can be used together with experiments to get a better interpretation of the physics underlying the flow phenomenon.

Actually, both the stable states of the flow, which lead to the formation either of an A-jump (at higher submergence and Froude number) or of a B-jump (at lower submergence and Froude number), and the flow conditions which exhibited an oscillatory pattern, with either an A-wave or a B-wave behaviour, were confirmed by the numerical results.

Although both turbulence models yielded similar results, the detailed comparison of the computed amplitude spectrum of the pressure fluctuations under hydraulic jump for the configuration with B-wave oscillations with the measured ones, showed that the results obtained with the simpler mixing-length model are even closer to the experimental data than the ones obtained with the standard k-ε model, in particular when amplitude spectra and peak amplitudes of the pressure fluctuations under hydraulic jump are compared.

As observed experimentally by [17], these numerical results show the existence of a peak at a similar frequency in the amplitude spectra of the time series of the surface elevations upstream and downstream of the jump, in the amplitude spectra of the pressure and in the amplitude spectra of the fluctuations of the velocity components measured under the hydraulic jump.

The analysis of amplitude spectra, of the vorticity fields and of the correlation coefficients indicates that velocity components and pressure fluctuations are strongly influenced by the oscillations between the B and wave jump types, and that a strong correlation exists among the velocity and vorticity fields and the pressure fluctuations even far downstream of the jump position.

Furthermore, these numerical results show that the oscillation between the B-jump and the stronger wave-jump tends to propagate its effects more than the oscillation between wave-jump and A-jump. In both cases, the waves generated by the oscillation show a remarkably non-linear behaviour while propagating in the flow direction.

The previous results show eventually that the SPH simulations can correctly reproduce all the main characteristics of this phenomenon, which under specific flow conditions can lead to cyclic oscillations between jump types, resulting in the cyclic formation and evolution of jump vortices. As such, the complete spatial and temporal knowledge of the flow yielded by the SPH simulation can improve the understanding of the phenomena, allowing one to perform detailed analyses directly on the numerical flow field, without resorting to additional, extensive experimental activity.

Author Contributions: M. Mossa. conceived and designed the experiments; M. Mossa performed the experiments; M.Mossa, D. De Padova and S. Sibilla analyzed the data; S. Sibilla developed the SPH numerical code; M. Mossa, D. De Padova and S. Sibilla contributed analysis tools; D. De Padova, M. Mossa and S. Sibilla wrote the paper.

Conflicts of Interest: The authors declare no conflict of interest.

References

1. Chow, V.T. *Open Channel Hydraulics*; McGraw-Hill: New York, NY, USA, 1959.
2. Rajaratnam, N.; Subramanya, K. Flow equation for the sluice gate. *J. Irrig. Drain. Eng.* **1967**, *93*, 167–186.
3. Moore, W.L.; Morgan, C.W. Hydraulic jump at an abrupt drop. *Trans. ASCE* **1959**, *124*, 507–524.
4. Hager, W.H.; Kawagoshi, N. Hydraulic jumps at rounded drop. *Proc. Instit. Civil Eng.* **1990**, *89*, 443–470. [CrossRef]
5. Ohtsu, I.; Yasuda, Y. Transition from supercritical to subcritical flow at an abrupt drop. *J. Hydraul. Res.* **1991**, *29*, 309–328. [CrossRef]
6. Chanson, H.; Toombes, L. Supercritical flowat an abrupt drop: Flow patterns and aeration. *Can. J. Civil. Eng.* **1998**, *25*, 956–966. [CrossRef]
7. Nebbia, G. Su taluni fenomeni alternativi in correnti libere. *L'Energia Elettrica, Fasc. I* **1942**, *XIX*, 1–10. Available online: http://www.diia.unina.it/pdf/pubb0034.pdf (accessed on 12 October 2017).
8. Hager, W.H.; Bretz, N.V. Hydraulic jumps at positive and negative steps. *J. Hydraul. Res.* **1986**, *24*, 237–252. [CrossRef]

9. Abdel Ghafar, A.; Mossa, M.; Petrillo, A. Scour from flowdownstream of a sluice gate after a horizontal apron. In Proceedings of the Sixth International Symposium on River Sedimentation—Management of Sediment—Philosophy, Aims, and Techniques, New Delhi, India, 7–11 November 1995; Varma, C.V.J., Rao, A.R.G., Eds.; Oxford & IBH Publishing Co. Pvt. Ltd.: Delhi, India, 1995; pp. 1069–1088.
10. Mossa, M.; Petrillo, A. Sui fenomeni alternativi in un risalto idraulico. In Proceedings of the Congress 'Giornate di Studio in onore del Prof. Edoardo Orabona nel centenario della nascita', Editoriale BIOS, Rome, Italy, 13-14 October 1997; pp. 125–153. (In Italian)
11. Mossa, M.; Tolve, U. Flow visualization in bubbly two-phase hydraulic jump. *J. Fluids Eng.* **1998**, *120*, 160–165. [CrossRef]
12. Mossa, M. On the oscillating characteristics of hydraulic jumps. *J. Hydraul. Res.* **1999**, *37*, 541–558. [CrossRef]
13. Wang, H.; Chanson, H. Experimental study of turbulent fluctuations in hydraulic jumps. *J. Hydraul. Eng.* **2015**, *141*, 04015010-1–04015010-10. [CrossRef]
14. Wang, H.; Murzyn, F.; Chanson, H. Total pressure fluctuations and two-phase flow turbulence in hydraulic jumps. *Exp. Fluids* **2014**, *55*. [CrossRef]
15. Long, D.; Rajaratnam, N.; Steffler, P.M.; Smy, P.R. Structure of flow in hydraulic jumps. *J. Hydraul. Res.* **1991**, *29*, 207–218. [CrossRef]
16. Mossa, M.; Petrillo, A.; Chanson, H. Tailwater Level Effects on Flow Conditions at an Abrupt Drop. *J. Hydraul. Res.* **2003**, *41*, 39–51. [CrossRef]
17. Chippada, S.; Ramaswamy, B.; Wheeler, M.F. Numerical simulation of hydraulic jump. *Int. J. Num. Meth. Eng.* **1994**, *37*, 1381–1397. [CrossRef]
18. Ma, F.; Hou, Y.; Prinos, P. Numerical calculation of submerged hydraulic jumps. *J. Hydraul. Res.* **2001**, *39*, 493–503. [CrossRef]
19. Carvalho, R.; Lemos, C.; Ramos, C. Numerical computation of the flow in hydraulic jump stilling basins. *J. Hydraul. Res.* **2008**, *46*, 739–752. [CrossRef]
20. Meireles, I.C.; Bombardelli, F.A.; Matos, J. Air entrainment onset in skimming flows on steep stepped spillways: An analysis. *J. Hydraul. Res.* **2014**, *52*, 375–385. [CrossRef]
21. Chanson, H.; Carvalho, R. Hydraulic jumps and stilling basins. Chapter 4. In *Energy Dissipation in Hydraulic Structures*; Chanson, H., Ed.; CRC Press, Taylor & Francis Group: Boca Raton, FL, USA, 2015; A. Balkema Book.
22. Bayon, A.; Valero, D.; García-Bartual, R.; Jos, F.; Valles-MorF, J.; Lopez-Jim, P. Performance assessment of OpenFOAM and FLOW-3D in the numerical modeling of a low Reynolds number hydraulic jump. *Environ. Model. Softw.* **2016**, *80*, 322–335. [CrossRef]
23. Dalrymple, R.A.; Rogers, B.D. Numerical modelling of waves with the SPH method. *Coast. Eng.* **2006**, *53*, 131–147. [CrossRef]
24. De Padova, D.; Dalrymple, R.A.; Mossa, M. Analysis of the artificial viscosity in the smoothed particle hydrodynamics modelling of regular waves. *J. Hydraul. Res.* **2014**, *52*, 836–848. [CrossRef]
25. Altomare, C.; Suzuki, T.; Domínguez, J.M.; Crespo, A.J.C.; Gómez-Gesteira, M.; Caceres, I. A hybrid numerical model for coastal engineering problems. In Proceedings of the 34th International Conference on Coastal Engineering (ICCE), Seoul, Korea, 15–20 June 2014. [CrossRef]
26. Lind, S.J.; Stansby, P.K.; Rogers, B.D.; Lloyd, P.M. Numerical predictions of water-air wave slam using incompressible-compressible smoothed particle hydrodynamics. *Appl. Ocean Res.* **2015**, *49*, 57–71. [CrossRef]
27. Ni, X.; Feng, W.B.; Wu, D. Numerical simulations of wave interactions with vertical wave barriers using the SPH method. Int. J. Numer. *Methods Fluids* **2014**, *76*, 223–245. [CrossRef]
28. Shadloo, M.S.; Weiss, R.; Yildiz, M.; Dalrymple, R.A. Numerical simulation of long wave runup for breaking and nonbreaking waves. *Int. J. Offshore Polar Eng.* **2015**, *25*, 1–7.
29. De Padova, D.; Mossa, M.; Sibilla, S. SPH numerical investigation of the velocity field and vorticity generation within a hydrofoil-induced spilling breaker. *Environ. Fluid Mech.* **2016**, *16*, 267–287. [CrossRef]
30. Fourtakas, G.; Rogers, B.D.; Laurence, D.R. Modelling sediment resuspension in industrial tanks using SPH. *La Houille Blanche* **2014**, *18*, 39–45. (In French) [CrossRef]
31. Manenti, S.; Sibilla, S.; Gallati, M.; Agate, G.; Guandalini, R. SPH simulation of sediment flushing induced by a rapid water flow. *J. Hydraul. Eng.* **2012**, *138*, 272–284. [CrossRef]

32. Manenti, S.; Pierobon, E.; Gallati, G.; Sibilla, S.; D'Alpaos, L.; Macchi, E.G.; Todeschini, S. Vajont disaster: Smoothed Particle Hydrodynamics modeling of the post-event 2D experiments. *J. Hydraul. Eng.* **2016**, *142*, 1–11. [CrossRef]
33. Mokos, A.; Rogers, B.D.; Stansby, P.K. Multiphase SPH modelling of violent hydrodynamics on GPUs. *Comput. Phys. Commun.* **2015**, *196*, 304–316. [CrossRef]
34. Ulrich, C.; Leonardi, M.; Rung, T. Multi-physics SPH simulation of complex marine-engineering hydrodynamic problems. *Ocean Eng.* **2013**, *64*, 109–121. [CrossRef]
35. Shadloo, M.S.; Oger, G.; Le Touzé, D. Smoothed particle hydrodynamics method for fluid flows, towards industrial applications: Motivations, current state, and challenges. *Comput. Fluids* **2016**, *136*, 11–34. [CrossRef]
36. Ataie-Ashtiani, B.; Shobeyri, G. Numerical simulation of landslide impulsive waves by incompressible smoothed particle hydrodynamics. *Int. J. Numer. Methods Fluids* **2008**, *56*, 209–232. [CrossRef]
37. Capone, T.; Panizzo, A.; Monaghan, J.J. SPH modelling of water waves generated by submarine landslides. *J. Hydraul. Res.* **2010**, *48*, 80–84. [CrossRef]
38. Cartwright, B.K.; Chhor, A.; Groenenboom, P. Numerical simulation of a helicopter ditching with emergency flotation devices. In Proceedings of the 5th Spheric International workshop, Manchester, UK, 23–25 June 2010; pp. 98–105.
39. Marrone, S.; Bouscasse, B.; Colagrossi, A.; Antuono, M. Study of ship wave breaking patterns using 3D parallel SPH simulations. *Comput. Fluids* **2012**, *69*, 54–66. [CrossRef]
40. Zhang, A.; Cao, X.-Y.; Ming, F.; Zhang, Z.-F. Investigation on a damaged ship model sinking into water based on three dimensional SPH method. *Appl. Ocean Res.* **2013**, *42*, 24–31. [CrossRef]
41. Espa, P.; Sibilla, S.; Gallati, M. SPH simulations of a vertical 2-D liquid jet introduced from the bottom of a free-surface rectangular tank. *Adv. Appl. Fluid Mech.* **2008**, *3*, 105–140.
42. López, D.; Marivela, R.; Garrote, L. Smoothed Particle Hydrodynamics Model Applied to Hydraulic Structures: A Hydraulic Jump Test Case. *J. Hydraul. Res.* **2010**, *48*, 142–158. [CrossRef]
43. Jonsson, P.; Jonsén, P.; Andreasson, P.; Lundström, T.; Hellström, J. Smoothed Particle Hydrodynamic Modelling of Hydraulic Jumps: Bulk Parameters and Free Surface Fluctuations. *Engineering* **2016**, *8*, 386–402. [CrossRef]
44. Federico, I.; Marrone, S.; Colagrossi, A.; Aristodemo, F.; Antuono, M. Simulating 2D open-channel flows through an SPH model. *Eur. J. Mech. B/Fluids* **2012**, *34*, 35–46. [CrossRef]
45. Chern, M.-J.; Syamsuri, S. Effect of Corrugated Bed on Hydraulic Jump Characteristic Using SPH Method. *J. Hydraul. Eng.* **2013**, *139*, 221–232. [CrossRef]
46. De Padova, D.; Mossa, M.; Sibilla, S.; Torti, E. 3D SPH modelling of hydraulic jump in a very large channel. *J. Hydraul. Res.* **2013**, *51*, 158–173. [CrossRef]
47. Ben Meftah, M.; De Serio, F.; Mossa, M.; Pollio, A. Analysis of the velocity field in a large rectangular channel with lateral shockwave. *Environ. Fluid Mech.* **2007**, *7*, 519–536. [CrossRef]
48. Ben Meftah, M.; De Serio, F.; Mossa, M.; Pollio, A. Experimental study of recirculating flows generated by lateral shock waves in very large channels. *Environ. Fluid Mech.* **2008**, *8*, 215–238. [CrossRef]
49. Ben Meftah, M.; Mossa, M.; Pollio, A. Considerations on shock wave/boundary layer interaction in undular hydraulic jumps in horizontal channels with a very high aspect ratio. *Eur. J. Mech. B/Fluids* **2010**, *29*, 415–429. [CrossRef]
50. Mossa, M. Discussion on Relation of surface roller eddy formation and surface fluctuation in hydraulic jumps by K.M. Mok. *J. Hydraul. Res.* **2005**, *43*, 588–592. [CrossRef]
51. Mossa, M.; Petrillo, A.; Chanson, H. Discussion on the "Tailwater Level Effects on Flow Conditions at an Abrupt Drop". Unpublished work. 2004.
52. Mossa, M. Experimental study of the flow field with spilling type breaking. *J. Hydraul. Res.* **2008**, *46*, 81–86. [CrossRef]
53. Gomez-Gesteira, M.; Rogers, B.D.; Darlymple, R.A.; Crespo, A.J.C. State-of-the-art of classical SPH for free-surface flows. *J. Hydraul. Res.* **2010**, *48*, 6–27. [CrossRef]
54. Liu, G.R.; Liu, M.B. *Smoothed Particle Hydrodynamics—A Meshfree Particle Methods*; World Scientific Publishing: 5 Toh Tuck Link, Singapore, 2007.
55. Monaghan, J.J. Smoothed particle hydrodynamics. *Annu. Rev. Astron. Astrophys.* **1992**, *30*, 543–574. [CrossRef]

56. Monaghan, J.J. Smoothed particle hydrodynamics. *Rep. Progress Phys.* **2005**, *68*, 1703–1759. [CrossRef]
57. Violeau, D. *Fluid mechanics and the SPH method: Theory and applications*; Oxford University Press: Oxford, UK, 2012.
58. Monaghan, J.J. Simulating free surface flows with SPH. *J. Comput. Phys.* **1992**, *110*, 399–406. [CrossRef]
59. Wendland, H. Piecewise polynomial, positive definite and compactly supported radial functions of minimal degree. *Adv. Comput. Math.* **1995**, *4*, 389–396. [CrossRef]
60. Sibilla, S. An algorithm to improve consistency in Smoothed Particle Hydrodynamics. *Comput. Fluids* **2015**, *118*, 148–158. [CrossRef]
61. Lind, S.; Xu, R.; Stansby, P.; Rogers, B.; Lloyd, P.M. Incompressible smoothed particle hydrodynamics for free-surface flows: A generalised diffusion based algorithm for stability and validations for impulsive flows and propagating waves. *J. Comput. Phys.* **2012**, *231*, 1499–1523. [CrossRef]
62. Khayyer, A.; Gotoh, H.; Shimizu, Y. Comparative study on accuracy and conservation properties of two particle regularization schemes and proposal of an optimized particle shifting scheme in ISPH context. *J. Comput. Phys.* **2017**, *332*, 236–256. [CrossRef]
63. Vacondio, R.; Rogers, B.; Stansby, P.; Mignosa, P. Variable resolution for SPH in three dimensions: Towards optimal splitting and coalescing for dynamic adaptivity. *Comput. Methods. Appl. Mech. Eng.* **2016**, *300*, 442–460. [CrossRef]
64. Sun, P.; Colagrossi, A.; Marrone, S.; Zhang, A. The δ+-SPH model: Simple procedures for a further improvement of the SPH scheme. *Comput. Methods Appl. Mech. Eng.* **2017**, *315*, 25–49. [CrossRef]
65. Antuono, M.; Colagrossi, A.; Marrone, S.; Molteni, D. Free-surface flows solved by means of SPH schemes with numerical diffusive terms. *Comput. Phys. Commun.* **2010**, *181*, 532–549. [CrossRef]
66. Antuono, M.; Colagrossi, A.; Marrone, S. Numerical diffusive terms in weakly-compressible SPH schemes. *Comput. Phys. Commun.* **2012**, *183*, 2570–2580. [CrossRef]
67. Meringolo, D.D.; Colagrossi, A.; Marrone, S.; Aristodemo, F. On the filtering of acoustic components in weakly-compressible SPH simulations. *J. Fluids Struct.* **2017**, *70*, 1–23. [CrossRef]
68. Aristodemo, F.; Tripepi, G.; Meringolo, D.D.; Veltri, P. Solitary wave-induced forces on horizontal circular cylinders: Laboratory experiments and SPH simulations. *Coast. Eng.* **2017**, *129*, 17–35. [CrossRef]
69. Kazemi, E.; Nichols, A.; Tait, S.; Shao, S. SPH modelling of depth-limited turbulent open channel flows over rough boundaries. *Int. J. Numer. Methods Fluids* **2017**, *83*, 3–27. [CrossRef] [PubMed]
70. Launder, B.E.; Spalding, D.B. The numerical computation of turbulent flows. *Comput. Methods Appl. Meth. Eng.* **1974**, *3*, 269–289. [CrossRef]
71. Violeau, D.; Issa, R. Numerical modelling of complex turbulent free-surface flows with the SPH method: An overview. *Int. J. Numer. Methods Fluids* **2007**, *53*, 277–304. [CrossRef]
72. Randles, P.W.; Libersky, L.D. Smoothed particle hydrodynamics: Some recent improvements and applications. *Comput. Methods Appl. Mech. Eng.* **1996**, *139*, 375–408. [CrossRef]
73. De Padova, D.; Dalrymple, R.A.; Mossa, M.; Petrillo, A.F. An analysis of SPH smoothing function modelling a regular breaking wave. In Proceedings of the International Conference XXXI Convegno Nazionale di Idraulica e Costruzioni Idrauliche, Perugia, Italy, 9–12 September 2008; p. 182.
74. Guza, R.T.; Thornton, E.B. Local and shoaled comparisons of sea surface elevations, pressures and velocities. *J. Geoph. Res.* **1980**, *85*, 1524–1530. [CrossRef]
75. Petrillo, A. Evoluzione delle onde di mare su bassi fondali sabbiosi con pendenza variabile. In Proceedings of the IX Congresso Nazionale AIMET A, Bari, Italy, 7–8 Ottobre 1988.